

Article

# Structural, Morphological, and Optical Properties of Iron Doped $\text{WO}_3$ Thin Film Prepared by Pulsed Laser Deposition

**Mariana Osiac** <sup>1,\*</sup>, **Nicoleta Cioatera** <sup>2</sup> and **Maria Jigau** <sup>1</sup><sup>1</sup> Department of Physics, Faculty of Science, University of Craiova, 200585 Craiova, Romania; mariajigau@mail.ru<sup>2</sup> Department of Chemistry, Faculty of Science, University of Craiova, 200585 Craiova, Romania; cioatera@yahoo.com

\* Correspondence: m\_osiac@yahoo.com

Received: 17 March 2020; Accepted: 16 April 2020; Published: 21 April 2020



**Abstract:** The iron doped tungsten-oxide (Fe and  $\text{WO}_3$ ) thin film with different morphology and crystalline structures were obtained for different substrate temperatures at the oxygen pressure of 14.66 Pa. The Fe-doped  $\text{WO}_3$  films were deposited by pulsed laser deposition (PLD). The influence of the substrate temperature on the surface and on the crystalline phases of the films was studied. The XRD (X-ray diffraction) analysis indicates the changing in the crystalline phases from  $\gamma$ -monoclinic to a mixture of  $\gamma$ -monoclinic and hexagonal phases dependent on the temperature of annealing and as-grown films. Related to the as-grown and annealing films conditions, the SEM (scanning electron microscopy) shows a change in the image surface from nanoneedles, to nanoporous, and further to long nanowires and broad nanobands. Energy-dispersive X-ray spectroscopy (EDX) shows the elemental composition of the Fe-doped  $\text{WO}_3$  film as-grown and after annealing treatment. Raman spectroscopy presented the main vibration mode of the Fe-doped  $\text{WO}_3$  thin film. The optical energy bandgap of the films is decreasing as the substrate temperature increases.

**Keywords:** tungsten trioxide; Fe-doped  $\text{WO}_3$ ; PLD method; structural and morphological characterization

## 1. Introduction

At present, since industrialization continues to advance, air pollution has become a topic of current interest for health, research, and detection of polluting gases. Detection of toxic gases from air is mainly done by gas sensors. Gas sensors should have some characteristics such as high sensitivity and selectivity, minimum concentration of detectable gases, fast response/recovery speed, reversibility, minimum energy consumption, and low fabrication cost [1]. Metal-oxide semiconductor thin films are important material because of their potential applications in photo-catalysis [2], solar cells, and gas sensors. Nanostructured metal oxide semiconductors thin films such as  $\text{WO}_3$ ,  $\text{SnO}_2$ ,  $\text{ZnO}$  and  $\text{In}_2\text{O}_3$  are intensively studied, being an important subject in the research field of resistivity type gas sensors, since the interaction between the analysts and sensing materials thin film of the surface lead to significant variation in the electrical resistivity. The tungsten trioxide ( $\text{WO}_3$ ) is an n-type semiconductor with a wide band gap of 2.5 to 3 eV and is commonly used as sensing material because it reacts to a large number of gas molecules and has a strong variation in resistance [3]. Similar to other semiconducting oxide such as  $\text{SnO}_2$ ,  $\text{ZnO}$  and  $\text{In}_2\text{O}_3$ , its film surface is characterized by the oxygen vacancies. Among metal oxide semiconductors, tungsten oxide is inexpensive and chemically stable with relatively high electrical conductivity. Tungsten oxide has been used in various fields as a gas, humidity and temperature sensors, optical modulation devices and flat panel displays [3–7]. Recently,

in gas sensing applications,  $\text{WO}_3$  has been tested against various concentrations of toxic gases, i.e., CO,  $\text{NO}_x$ ,  $\text{SO}_2$ ,  $\text{H}_2\text{S}$ ,  $\text{NH}_3$  and acetone [8–18]. Therefore, In-doped  $\text{WO}_3$  sensors [19] have been observed to have high response to acetone, while Fe-doped  $\text{WO}_3$  [20] had good sensing performance to ethanol at room temperature. An optimal response to  $\text{NO}_2$  gas were tests with Sb-doped  $\text{WO}_3$  sensors [21]. Moreover, the gas sensing properties of the prepared Fe–C-co-doped  $\text{WO}_3$  spheres were tested and the effects of working temperature and Fe content on the responses to acetone were optimized. It was proposed the synthesized hierarchical  $\text{WO}_3$  microspheres film with the combined effect of Fe–C co-doping in  $\text{WO}_3$  improved the sensitivity and selectivity of acetone [22]. To enhance the gas sensing performance, doping with various dopants such as Ag [23], Pd [14,18,24], Pt [13,16] and Fe [17,20] is an effective method to introduce oxygen vacancies in the structure of oxides. Moreover, to improve the gas-sensing performance of  $\text{WO}_3$  many attempts have been done to obtain films with different morphologies, i.e., nanoparticles [25], nanofibers [26], nanorods [6], nanoneedles [27], nanotubes [28], nanosheets [28,29], and core-shell microspheres [30]. It is known that certain diseases are associated with specific inorganic gases and volatile organic compounds (VOCs) in human breath. Particularly, diabetes, which is seriously harmful to human health, can be diagnosed by acetone detection from human breath. Detection and monitoring the illness by breath, in the early stages, drastically reduce the diagnostic medical costs and improve the quality of life of patients suffering from chronic illnesses. In addition, acetone is a type of toxic and explosive gas, and it is used in industries and labs, being harmful to health. Several metal oxides such as  $\text{Fe}_2\text{O}_3$  [5,30],  $\text{In}_2\text{O}_3$  [31],  $\text{WO}_3$  [32] and a portable Si-doped  $\text{WO}_3$  nanostructured [31–33], have been used to distinguish the diabetic from the healthy by detecting the acetone concentration. Another organic compound such as formaldehyde (HCHO), which has a carcinogenic nature, is a gas that is hazardous for the environment, and its detection is always important in biomedical applications and food industries [34–37]. Ethanol ( $\text{C}_2\text{H}_5\text{OH}$ ), an inflammable volatile organic compound, is most extensively used as alcohol, with many applications in the food and chemical industries, biomedical as well as health and safety. The Occupational Safety Health and Administration (OSHA) has established that the maximum exposure level of the ethanol to be 1000 ppm, since exposure to ethanol vapor causes health problems such as difficulties in breathings, headaches, drowsiness, irritation of the eyes, and liver damage [36–39]. In this regard, considerable efforts have been done to improve the ethanol sensing performances such as sensitivity and selectivity of  $\text{WO}_3$  sensors due to its electrochromic properties [38]. Moreover, heterojunction formation between the n- $\text{WO}_3$  and p- $\text{CrO}_3$  improve the gas sensing properties of  $\text{WO}_3$  nanorods for ethanol detection [39]. In literature, proposed many techniques of deposition of  $\text{WO}_3$  and doped  $\text{WO}_3$  sensing layer for detection of polluting gases have been proposed, such as hydrothermal method [3,6], sonochemical preparation [8], pulsed laser deposition [7,23], electrospinning [26], and sol-gel [38].

Since the thin film is a sensing material, which is the main part of the sensor, the aim of this paper is to study the structural, morphological, and optical characterization of the Fe-doped  $\text{WO}_3$  film. In literature, there are few papers regarding the Fe-doped  $\text{WO}_3$  as a sensing layers [17,20] and its characterization is required. The deposition method proposed here was pulsed laser deposition (PLD). The crystallinity, composition, and morphology of the film were investigated using XRD in thin film configuration (GIXRD—grazing incidence X-ray), SEM coupled with EDX and Raman spectroscopy. The optical properties (diffuse reflectance) were measured with Analytik Jena Specord 210 plus spectrophotometer equipped with an integrating sphere and a Spectralon reflectance standard.

## 2. Methods

The  $\text{WO}_3$  and Fe-doped  $\text{WO}_3$  thin films were deposited on the silicon substrates by PLD. PLD consists of a YAG:Nd laser working on the fifth harmonic frequency (215 nm, 10 ns pulse length, 10 Hz repetition rate). The laser radiation was focused on a rotating target of  $\text{WO}_3$  (purity 99.9%) and Fe (purity 99.8%), respectively, in sectorial deposition. The sectorial deposition was used to introduce Fe in the thin film. The substrate was rotating during deposition and the laser fluence was kept constant at  $3 \text{ J/cm}^2$ . The first sample S1, Fe-doped  $\text{WO}_3$  film was deposited to a substrate temperature of  $600^\circ\text{C}$  and

then it was annealed to 700, 720, and 750 °C, respectively. The second sample S2, Fe-doped  $\text{WO}_3$  film has been deposited at 720 °C and it was annealing at 750 °C. The oxygen pressure during deposition and annealing treatment was kept constant at 14.66 Pa. The distance between target and substrate was 4.5 cm. The thickness of the film was 150 nm. The deposition and the annealing treatment were done 4 h in oxygen atmosphere. The temperature rate in annealing treatment was 15 °C/min similar to the deposition process.

The crystalline structure of the  $\text{WO}_3$  and Fe-doped  $\text{WO}_3$  samples was investigated by X-ray diffraction Szimadzu 6000 system, the morphology surface by SEM coupled with EDX, a Hitachi system, (Hitachi Ltd., Tokyo, Japan). The Raman spectroscopy (Renishaw system, Renishaw UK Ltd., New Mills, UK) with an excitation laser source of 785 nm, presented the vibration mode of  $\text{WO}_3$  and Fe-doped  $\text{WO}_3$  samples. The optical properties of the Fe-doped  $\text{WO}_3$  film samples were investigated by Analytik Jena Specord 210 plus (Analytik-Jena AG, Jena, Germany) in the wavelength region of 200 to 1200 nm.

### 3. Results

The results of this paper are presented in the following way: S1—the Fe-doped  $\text{WO}_3$  thin film was deposited at oxygen pressure of 14.66 Pa and temperature of 600 °C; this sample was subsequently annealed at temperature of 700, 720, and 750 °C, respectively; S2—the Fe-doped  $\text{WO}_3$  thin film was deposited at oxygen pressure of 14.66 Pa and temperature of 720 °C and then it was annealed at 750 °C. To compare the phase structure results of Fe-doped  $\text{WO}_3$  films, the  $\text{WO}_3$  thin film was deposited in oxygen pressure 14.66 Pa and temperature of 600 °C.

The phase and crystalline structure of the  $\text{WO}_3$  and Fe-doped  $\text{WO}_3$  samples, respectively presented in Figure 1, have been identified by GIXRD. The X-ray pattern of  $\text{WO}_3$  thin film is indexed to  $\gamma$ -monoclinic structure (JCPDS card 01-083-0950), with the diffraction peaks characteristic to reflection planes (002), (020), and (200), respectively. The diffraction peaks of the  $\text{WO}_3$  corresponding to reflection planes of (002), (020), and (200), respectively, are in good agreement with reported diffractograms for  $\gamma\text{-}\text{WO}_3$  and  $\delta\text{-}\text{WO}_3$  (triclinic) phases. These two phases are very similar with respect to angular distortions and atomic distances, and they are expected to have similar thermodynamic stability [40]. The positions of the reflection planes of  $\text{WO}_3$  film are  $2\theta = 23.13^\circ$  (002),  $2\theta = 23.6^\circ$  (020) and  $2\theta = 24.42^\circ$  (200), respectively.

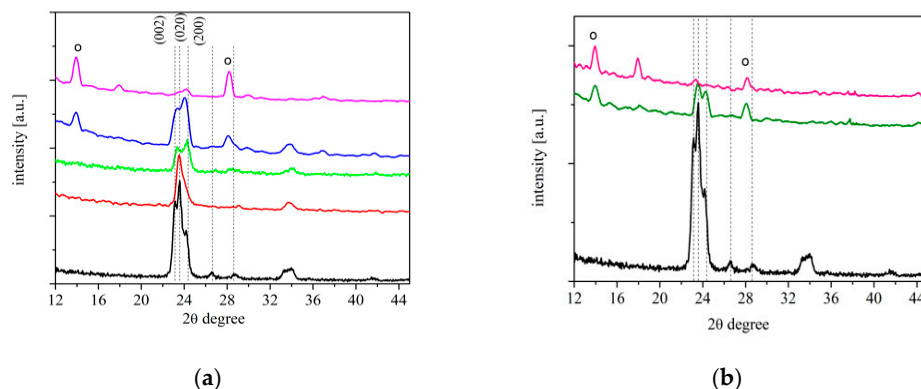


**Figure 1.** The GIXRD pattern for  $\text{WO}_3$  and Fe-doped  $\text{WO}_3$  thin films, respectively. (a) S1 sample: the red spectrum corresponds to S1 grown at  $T = 600$  °C; the green, blue, and magenta spectra belong to S1 samples annealed at  $T = 700$ , 720, and  $T = 750$  °C, respectively. (b) S2 sample: the dark green spectrum belongs to S2 grown at 720 °C and the pink spectrum corresponds to S2 annealed to 750 °C, respectively. The black spectrum corresponds to  $\text{WO}_3$  deposited at  $T = 600$  °C. The dotted lines show the  $\gamma$ -monoclinic plane positions of  $\text{WO}_3$ . The circles correspond to hexagonal phase.

The S1 sample grown at temperature of 600 °C show a  $\gamma$ -monoclinic crystalline phase with main preferential orientation along the (002) plane direction, slightly shifted to 23.54 degree [7,24]. The S1

sample was annealed at temperature of 700 °C and the peaks are observed at  $2\theta = 23.54^\circ$  and  $24.28^\circ$ , closely to the crystalline  $\gamma$ -monoclinic phases with (002) and (200) planes, respectively. The dominant peak at  $2\theta = 24.28^\circ$  could be a mixture of (020) and (200) planes. Increasing the annealing temperature of the S1 sample at 720 °C the crystalline structure presents a mixture of  $\gamma$ -monoclinic and hexagonal phases. The diffraction peaks corresponding to (100) and (200) plane, respectively belong to hexagonal structure (JCPDS card 00-007-2322). When the temperature is increased to 720 °C, the film still holds the stable  $\gamma$ -monoclinic phase indicating a well-defined crystalline structure and the presence of stoichiometric hexagonal is appeared. Further annealing of the S1 sample to 750 °C show a hexagonal phase while the  $\gamma$ -monoclinic phase almost disappeared.

The thin film of S2 sample grown at temperature of 720 °C show a hexagonal phase with (002) and (110) planes, respectively. The plane (002) is slightly shifted to  $\gamma$ -monoclinic; therefore, a minor mixing of the hexagonal and monoclinic phase could occur merely for the film grown to 720 °C. Increasing the annealing temperature to 750 °C the hexagonal phase is presented and the  $\gamma$ -monoclinic phase nearly vanished. The structure of hexagonal  $\text{WO}_3$  is not maintained without some stabilizing ions or molecules in the hexagonal channels, and thus the existence of strictly stoichiometric hexagonal  $\text{WO}_3$  is uncertain [41]. Consequently, the S1 sample annealed at temperature of 700 °C show the same crystalline structure as  $\text{WO}_3$  film. Similar crystalline structures were observed between pure  $\text{ZnO}$  and Fe-doped  $\text{ZnO}$ , where the small amount of Fe did not change the structure of  $\text{ZnO}$  but has a small influence on the crystallinity [41]. In the present case, Fe-doped  $\text{WO}_3$  thin film contains a small amount of Fe according to EDX measurements. Therefore, it is supposed that the Fe enter in the  $\text{WO}_3$  host lattice, and traces of any diffraction peaks associated with crystalline structure of iron or iron oxides are not observed. The small shift observed in the present GIXRD, for the S1 to 600 and 720 °C, at  $2\theta = 23.54^\circ$  is due to amount of Fe-doped  $\text{WO}_3$ . The structure and temperature for deposition and annealing of the samples S1, S2, and  $\text{WO}_3$  film, respectively, are presented in Table 1.

**Table 1.** The structure and temperature of S1, S2 film samples and  $\text{WO}_3$ , respectively.

Sample	Temperature Grown Film	Temperature Annealed Film	XRD Structure/Plane Positions
S1 (Fe-doped $\text{WO}_3$ )	600 °C	-	$\gamma$ -monoclinic $2\theta = 23.54^\circ$ (002)
	-	700 °C	$\gamma$ -monoclinic $2\theta = 23.54^\circ$ (002), $2\theta = 24.28^\circ$ (200)
	-	720 °C	$\gamma$ -monoclinic $2\theta = 23.54^\circ$ (002), $2\theta = 24.28^\circ$ (200) hexagonal $2\theta = 13.96^\circ$ (100), $2\theta = 28.13^\circ$ (200)
S2 (Fe-doped $\text{WO}_3$ )	-	750 °C	hexagonal phase
	720 °C	-	$\gamma$ -monoclinic $2\theta = 23.54^\circ$ (002), $2\theta = 24.28^\circ$ (200) hexagonal $2\theta = 13.96^\circ$ (100), $2\theta = 28.13^\circ$ (200)
	-	750 °C	hexagonal $2\theta = 13.96^\circ$ (100), $2\theta = 28.13^\circ$ (200)
$\text{WO}_3$ film	600 °C	-	$\gamma$ -monoclinic $2\theta = 23.13^\circ$ (002), $2\theta = 23.6^\circ$ (020), $2\theta = 24.42^\circ$ (200)

Since the radius of  $\text{Fe}^{3+}$  is almost similar to that of  $\text{W}^{6+}$ , a small distortion in the crystal lattice is observed to the  $\text{WO}_3$  doped with Fe. In this case a small shift in the diffraction peaks is present and a number of defects in the film could also be produced, making this film a better candidate for a gas detecting [22,42]. Likewise, the  $\text{W}^{6+}$  is octahedral coordinated with  $\text{O}^{2-}$ , and in the crystal of iron

oxide the field stabilization energy of  $\text{Fe}^{3+}$  is higher for octahedral orientation than for tetrahedral orientation. Consequently,  $\text{Fe}^{3+}$  can fulfil the same coordination as that of  $\text{W}^{6+}$ , and the Fe-doped  $\text{WO}_3$  film presents the same crystal structure as  $\text{WO}_3$  film.

The surface morphology of the Fe-doped  $\text{WO}_3$  samples deposited at oxygen pressure of 14.66 Pa and various substrate temperature range between 600 and 750 °C, respectively, are shown in Figure 2. The surface morphology for the samples deposited at temperatures of 600 and 650 °C, is nearly similar presented in nanoneedles shape. An increase in the temperatures to 700 and 720 °C, respectively, during deposition the nanoneedles on the sample surface, are distorted into nanowires grown on small nanobands. At the high temperature of 750 °C, the nanobands became thicker and shorter and started to agglomerate, making a porous surface morphology.

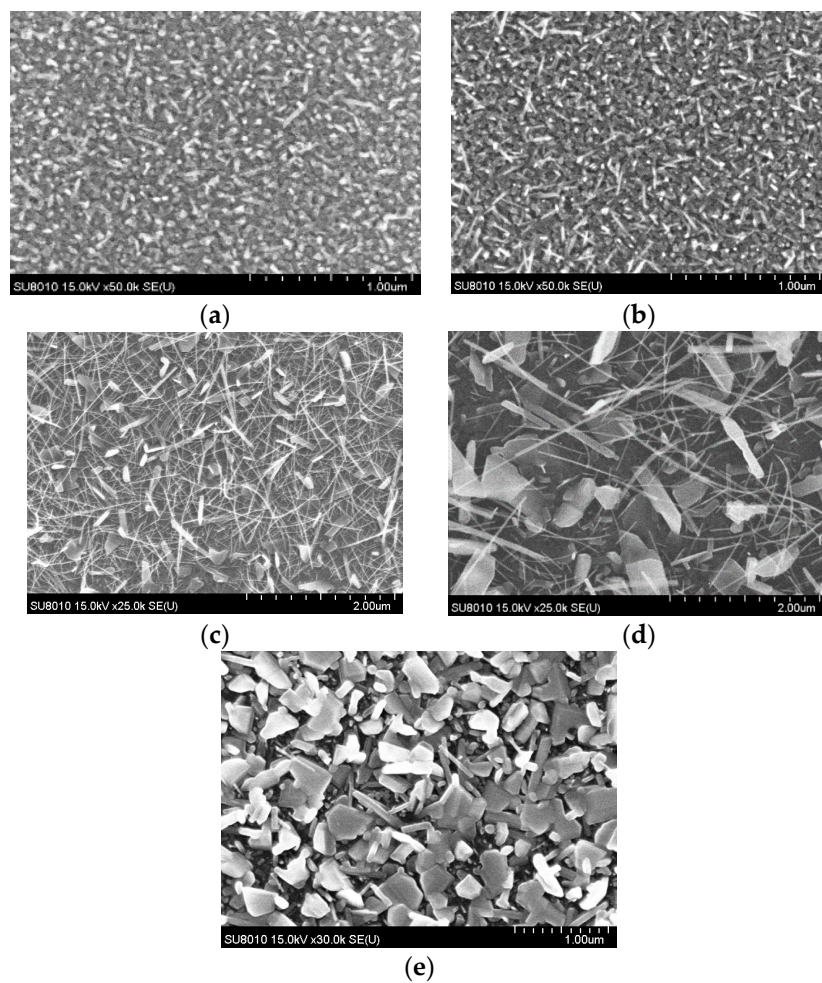


**Figure 2.** The top view topography of the Fe-doped  $\text{WO}_3$ : (a) the surface of the film grown at  $T = 600\text{ }^{\circ}\text{C}$ , (b)  $T = 650\text{ }^{\circ}\text{C}$ , (c)  $T = 700\text{ }^{\circ}\text{C}$ , (d)  $T = 720\text{ }^{\circ}\text{C}$ , (e)  $T = 750\text{ }^{\circ}\text{C}$ .

Besides the growing of Fe-doped  $\text{WO}_3$  at various temperatures, an annealing of the surface morphology for S1 sample deposited at oxygen pressure of 14.66 Pa and temperature of 600 °C has been investigated by SEM. The S1 sample annealed at temperature of 700 and 720 °C, respectively, presented in Figure 3b,c, shows a porous nanostructured surface that is well crystallized and consistent with the GIXRD measurements. There is not a large modification in the morphology surface between the samples annealed at 700 and 720 °C, respectively, since the temperature difference is small. Further annealing treatment at 750 °C change the surface morphology significantly, long, and thinner nanowires started to grow on the nanostructured surface as shown in Figure 3d.

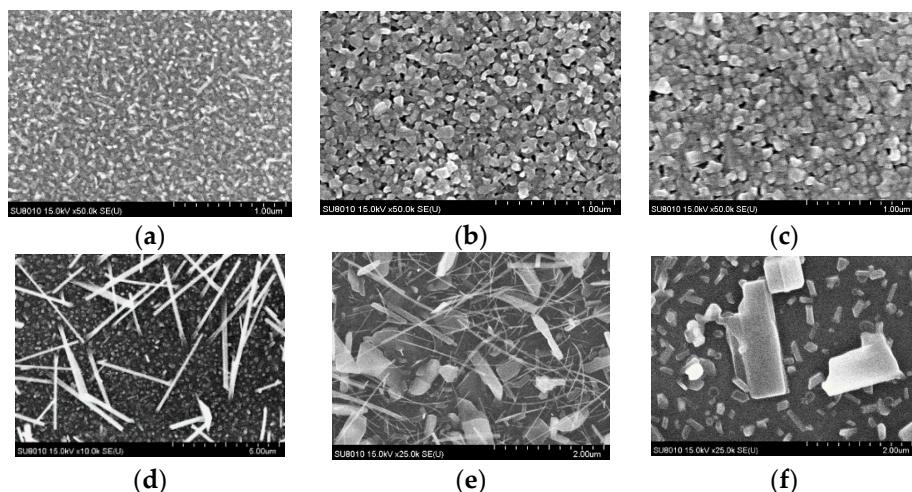


**Figure 3.** The top view topography of the Fe-doped  $\text{WO}_3$ : (a) S1 sample—the surface of the film grown at  $T = 600\text{ }^{\circ}\text{C}$ , (b) the film annealed at  $T = 700\text{ }^{\circ}\text{C}$ , (c) the film annealed at  $T = 720\text{ }^{\circ}\text{C}$ , (d) the film annealed at  $T = 750\text{ }^{\circ}\text{C}$ , (e) S2 sample—the film grown at  $720\text{ }^{\circ}\text{C}$ , (f) the film annealed at  $750\text{ }^{\circ}\text{C}$ .

The nanowires are grown over the nanostructured surface and they could be done by the surface oxidation during the annealing process. The S2 sample grown at temperature of  $720\text{ }^{\circ}\text{C}$  in oxygen pressure of  $14.66\text{ Pa}$  presented in Figure 3e, show a morphology surface formed by nanobands and very thin nanowires. An annealing of the S2 sample to a temperature of  $750\text{ }^{\circ}\text{C}$  changed the surface morphology to large and small nanobands. During annealing process at high temperature of  $750\text{ }^{\circ}\text{C}$  the nanowires vanished and thicker and shorter nanobands occurred. In the annealing treatment at this temperature, the oxygen atmosphere encourages the coalescence process of the thin nanowires to grow into nanobands. The samples grown and annealed at various temperatures change not only the crystalline phases but could significantly modify the film surface morphology.

According to the EDX measurements on the elemental composition in atomic percentages over the entire Fe-doped  $\text{WO}_3$  film of S1 and S2 samples is: O 40.88 at.%, Fe 0.35 at.% and W 58.77 at.%, respectively.

The EDX measurements of the S1 sample annealed at  $750\text{ }^{\circ}\text{C}$  are presented in Figure 4a,b. Figure 4a shows the EDX mapping on the film surface among the nanowires. The film surface is mainly formed by  $\text{WO}_3$ . The elemental composition presented in Table 2 show the existence of tungsten (W) and tungsten oxide on the film surface. The formation of nanowires appeared as a gradual structural transformation of the film involved nucleation on the oxidation film surface.

**Table 2.** The elemental composition of film surface presented in Figure 3a.

Element	O	W
Weight %	3.73	96.27
Atomic %	30.78	69.22

In the selected points on the long nanowires and among them, presented in Figure 4b, the  $\text{WO}_3$  composition is dominated. A tiny Fe distribution appeared only in few points. In the present work, we supposed that long nanowires are grown on the nucleation center after surface oxidation during annealing process. Under oxygen, the nucleation site is grown and results in crystalline nanowire configuration, according to GIXRD hexagonal phase. The Fe dopant did not represent a nucleation center. Table 3 presented the elemental composition of the several points on the film surface.

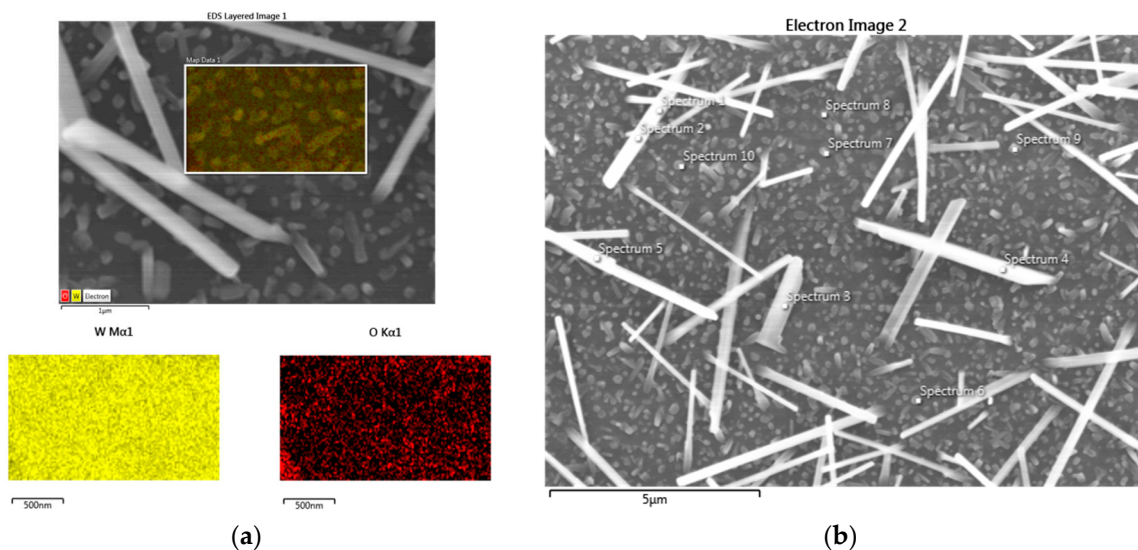


**Figure 4.** The image of the S1 sample annealed at 750 °C; (a) the EDX mapping between the nanowires, (b) 10 EDX points selected on the surface.

**Table 3.** The elemental composition of the S1 sample annealed at T = 750 °C, in the selected points.

Composition	Element	Spectrum									
		1	2	3	4	5	6	7	8	9	10
Weight %	O	10.12	3.61	7.32	3.03	13.82	6.39	3.94	3.33	2.65	3.11
	Fe	0.39	0.47	-	-	-	0.75	-	-	-	0.79
	W	89.49	95.92	92.68	96.97	86.18	92.86	96.06	96.67	97.33	96.1
Atomic %	O	56.15	29.85	47.59	26.44	64.83	43.51	32.02	28.35	23.86	26.58
	Fe	0.62	1.11	-	-	-	1.46	-	-	-	1.93
	W	43.23	69.04	52.41	73.56	35.17	1.46	67.98	71.65	76.14	71.49

The EDX mapping made on a large nanoband, presented in Figure 5a shows a distribution of W and O, almost similar to the long nanowires grown on the S1 sample, but with a large difference amount of W and O. The elemental composition of the large nanoband is shown in Table 4.

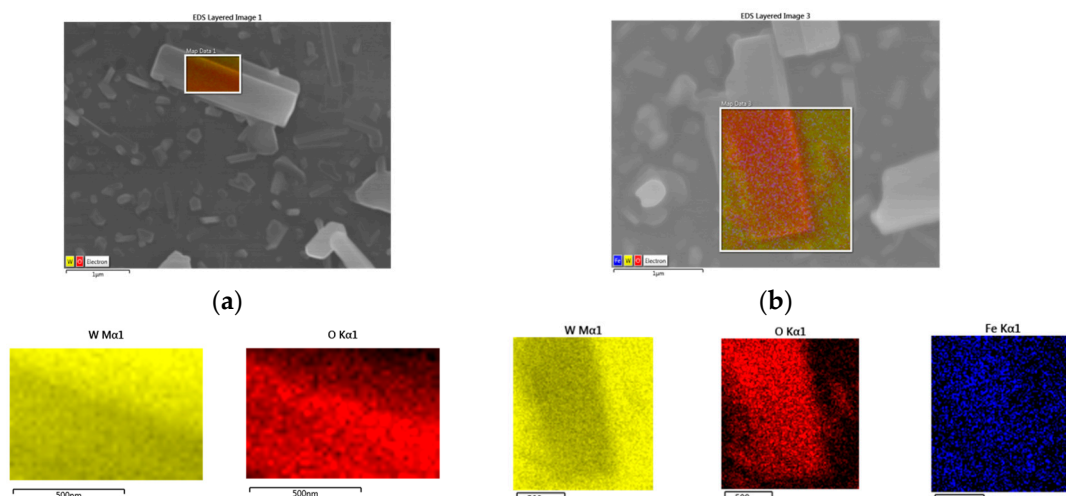


**Figure 5.** The EDX mapping of the S2 sample at T = 750 °C. (a) EDX mapping on a large nanoband; (b) EDX mapping made on a large nanoband and slice of the film surface.

**Table 4.** The elemental composition of the S2 sample annealed at  $T = 750\text{ }^{\circ}\text{C}$ , on the large nanoband, and large nanoband with a slice of the film surface.

EDX Mapping on a Large Nanoband			EDX Mapping on a Nanoband and a Slice of Film Surface		
Element	O	W	O	W	Fe
Weight %	12.15	87.85	7.94	91.87	0.19
Atomic %	61.38	38.62	46.67	50	0.33

The EDX mapping on the large nanoband and a slice of film surface, presented in Figure 5b, shows the Fe distribution merely on the film surface. The elemental composition film presented in Figure 5b is shown in Table 4, second column. The EDX mapping show that the film is gradually converted from the thin nanowires and small nanobands into large nanobands during annealing treatment in the oxygen. It seems that the temperature is a critical parameter of the surface morphology. The actual shape of the S1 and S2 samples morphology surface is strongly dependent on the temperature higher than  $700\text{ }^{\circ}\text{C}$ . Changes in surface morphology formation proposed that the surface film is mainly metallic W, because of its heavy mass and low diffusivity, and a small amount of WO on the surface exists, according to EDX measurements. Related to GIXRD measurements, at a temperature of  $750\text{ }^{\circ}\text{C}$ , the  $\text{WO}_3$  oxide exists on the film surface in a hexagonal phase, but in the present work, we do not exclude the formation of sub-stoichiometric  $\text{WO}_{3-x}$  oxides.

Raman scattering is very sensitive to microstructure of nanocrystalline materials, so it was employed to determine the nanostructure of the Fe-doped  $\text{WO}_3$  films. The Raman spectra of  $\text{WO}_3$  show three vibration modes, at a lower wavenumber than  $250\text{ cm}^{-1}$ , to an intermediate wavenumber of  $200$  to  $400\text{ cm}^{-1}$  and at higher wavenumber of  $600$  to  $900\text{ cm}^{-1}$ , respectively. The vibrational modes at a lower wavenumber than  $250\text{ cm}^{-1}$  belong to  $\text{WO}_3$  lattice, i.e., translational and vibrational motion of  $\text{WO}_6$  octahedral in the same cell of unit. The vibrational modes in the intermediate wavenumber of  $200$  to  $400\text{ cm}^{-1}$  are attributed to bending modes of O–W–O bridging bonds. At higher wavenumber region of  $600$  to  $900\text{ cm}^{-1}$ , the vibrational mode is attributed to the O–W–O stretching bonds [43].

The Raman peak presented in Figure 6a, for the  $\text{WO}_3$  film grown at  $600\text{ }^{\circ}\text{C}$  is located at  $810\text{ cm}^{-1}$ . In Figure 6a, the large Raman peak located to  $810\text{ cm}^{-1}$  is observed for the S1 samples annealed at  $700$  and  $720\text{ }^{\circ}\text{C}$ , respectively. A very sharp Raman peak located at  $810\text{ cm}^{-1}$  for the S2 sample grown at  $720\text{ }^{\circ}\text{C}$  is shown in Figure 6b. These features are characteristic to the O–W–O stretching vibration modes of  $\gamma$ -monoclinic  $\text{WO}_3$  phase, in accordance with GIXRD measurements. The presence of Raman peaks at low and intermediate wavenumber is not clearly noticeable by the Si and Si–O bonds of Si substrate. The sharp peak of Si is not presented in the Figure 6. The peaks observed at  $622$  and  $670\text{ cm}^{-1}$ , respectively, belong to the Si–O bonds of Silicon substrate [44]. Two Raman peaks are observed for the S1 and S2 samples annealed at  $750\text{ }^{\circ}\text{C}$  in Figure 6b. These peaks are located at  $735$  and  $791\text{ cm}^{-1}$ , respectively and correspond to O–W–O stretching vibration mode. For the S2 sample as-grown at  $720\text{ }^{\circ}\text{C}$ , presented in Figure 6b, a small Raman peak is centered at  $136\text{ cm}^{-1}$  and is ascribed to  $\text{WO}_3$  lattice vibration. At higher wavenumber, Raman peaks located to  $714$  and  $810\text{ cm}^{-1}$ , respectively, are assigned to O–W–O stretching vibration modes of monoclinic  $\gamma$ - $\text{WO}_3$  phase in accordance with the GIXRD measurements. In Figure 6b, in a higher wavenumber range, a shift of  $21\text{ cm}^{-1}$  is observed between the Raman peaks of the S2 sample as-grown at  $720\text{ }^{\circ}\text{C}$  and samples S1 and S2 annealed at  $750\text{ }^{\circ}\text{C}$ . A comparison of the Raman peaks for both samples is presented in Table 5. Such a shift could be connected with the shortening of stretching vibration modes O–W–O, which corresponds either to small cell parameters of Fe-doped  $\text{WO}_3$  or most likely to the hexagonal phase of the Fe-doped  $\text{WO}_3$  annealed at  $750\text{ }^{\circ}\text{C}$  in agreement to GIXRD measurements. No vibration mode connected with the  $\text{Fe}_2\text{O}_3$  is observed in the present measurements, since the quantity of Fe is low (less than 1 at.%) and enter in the structure of  $\text{WO}_3$  host lattice. The lack of the Raman peak at  $950\text{ cm}^{-1}$  show a high crystallization nature of films.

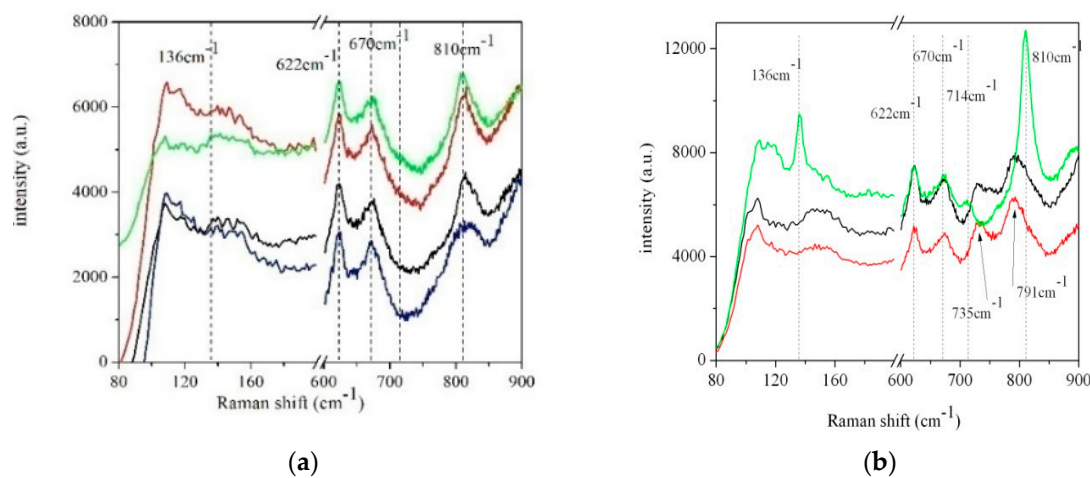


**Figure 6.** Raman spectra of  $\text{WO}_3$  and Fe-doped  $\text{WO}_3$  films. (a) the black spectrum belongs  $\text{WO}_3$  film grown at  $600\text{ }^\circ\text{C}$ ; the blue spectrum belongs to S1 sample grown at  $600\text{ }^\circ\text{C}$ ; the red and green spectra belong to S1 sample annealed at  $700$  and  $720\text{ }^\circ\text{C}$ , respectively. (b) the red spectrum belongs to S1 sample annealed at  $750\text{ }^\circ\text{C}$ , the green spectrum to S2 sample as-grown at  $720\text{ }^\circ\text{C}$  and the black spectrum to S2 sample annealed at  $750\text{ }^\circ\text{C}$ .

**Table 5.** Comparison of Raman peak positions of  $\text{WO}_3$  film and S1, S2 samples (Fe-doped  $\text{WO}_3$ ).

Samples	Raman Peaks Position ( $\text{cm}^{-1}$ )		
	Stretching Mode	Lattice Mode	
<b>Undoped Film</b>	$\text{WO}_3$ film grown at $60\text{ }^\circ\text{C}$	810	-
S1	Film grown at $600\text{ }^\circ\text{C}$	810	-
S1	Film annealed at $700\text{ }^\circ\text{C}$	810	-
S1	Film annealed at $720\text{ }^\circ\text{C}$	810	-
S1	Film annealed at $750\text{ }^\circ\text{C}$	791	735
S2	Film grown at $720\text{ }^\circ\text{C}$	810	714
S2	Film annealed at $750\text{ }^\circ\text{C}$	810	714
Shift	-	$21\text{ cm}^{-1}$	$21\text{ cm}^{-1}$

The optical band gap of Fe-doped  $\text{WO}_3$  film has been estimated with the help of Tauc Plot:  $F(R)$  versus photon energy ( $h\nu$ ), in which the Kubelka-Munk function,

$$F(R) = \frac{(1 - R)^2}{2R}, \quad (1)$$

where  $R$  is the diffuse reflectance. The optical band gap is obtained by extrapolating the linear part of  $(F(r)h\nu)^2$  plots to the energy axis. The  $(F(r)h\nu)^2$  plots versus photon energy are presented in Figure 7.

Table 6 shows the  $E_g$  of the Fe-doped  $\text{WO}_3$  for annealed and as-grown films.

**Table 6.** A comparison of the  $E_g$  for  $\text{WO}_3$  and S1 and S2 samples.

Sample	$E_g(\text{eV})$	Fe at.% According EDX	Surface Morphology
S1	Fe-doped $\text{WO}_3$ annealed to $720\text{ }^\circ\text{C}$	2.52	Nanostructured film
S2	Fe-doped $\text{WO}_3$ grown at $720\text{ }^\circ\text{C}$	2.32	Nanowires and nanobands
Undoped Film	$\text{WO}_3$ grown at $600\text{ }^\circ\text{C}$	3.30	Nanostructured film

A decrease in the optical band gap, particularly by temperature in the presence of oxygen vacancies or other structural defects such as voids, is presented in Table 6. Moreover,  $\text{WO}_3$  with Fe as dopant results in a small distortion of the  $\text{WO}_3$  crystalline structure, which reduces the optical band gap.

The optical band gap of deposited and annealing samples at 720 °C is smaller than optical band gap of undoped sample. This difference for the optical band gap could not be done merely to doping with Fe, but most likely to the effect of the surface oxidation during annealing in oxygen. In addition, the measurements of the optical band gaps show the effect of quantum confinement in the  $\text{WO}_3$  samples. This effect is obvious for Fe-doped  $\text{WO}_3$  annealed samples over 700 °C. Based on this effect, the optical band gap is reduced with the increase of grain sizes by annealing.

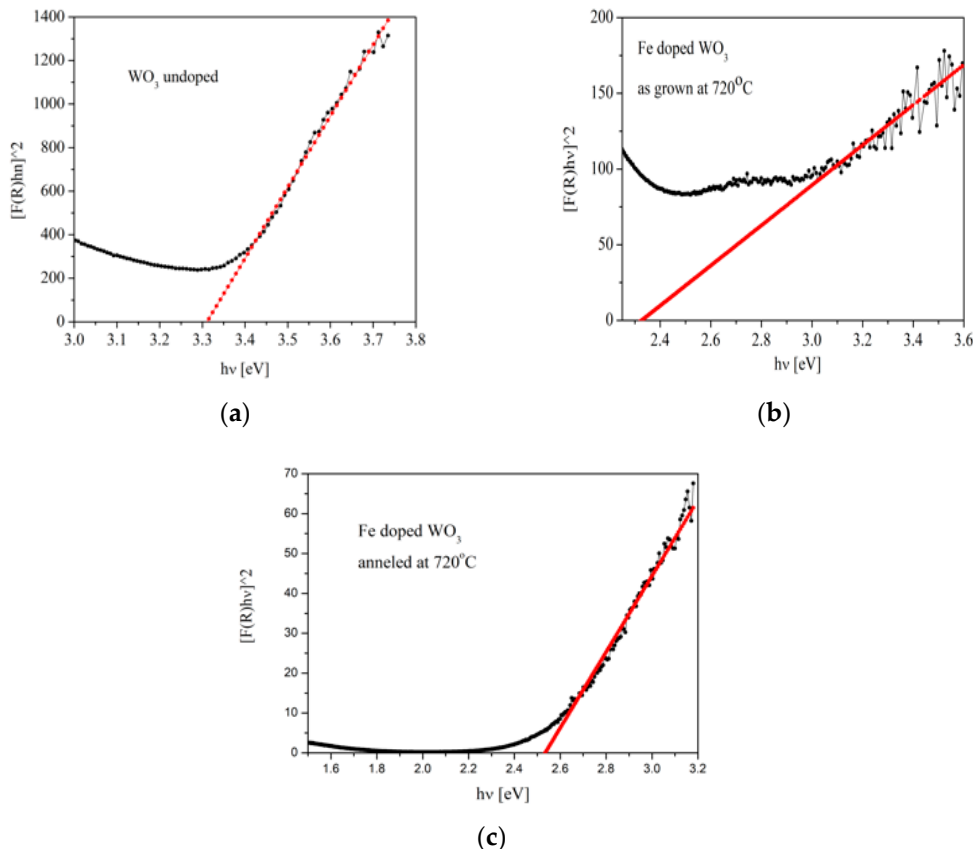


**Figure 7.** The  $E_g$  for  $\text{WO}_3$  film and Fe-doped  $\text{WO}_3$  film samples. (a)  $\text{WO}_3$  film grown at 600 °C (undoped); (b) Fe-doped  $\text{WO}_3$  as-grown at 720 °C; (c) Fe-doped  $\text{WO}_3$  annealed at 720 °C.

#### 4. Conclusions

The crystalline structure and the morphology thin film depend on deposition and annealing conditions and are easily controlled by PLD. The GIXRD results indicate a  $\gamma$ -monoclinic structure for  $\text{WO}_3$  thin film and a preferred orientation growth of a  $\gamma$ -monoclinic crystalline structure for the S1 sample grown at 600 °C and annealed at 700 °C, respectively. The Fe-doped  $\text{WO}_3$  film annealed at 720 °C show a  $\gamma$ -monoclinic structure mixed with hexagonal phase. When the annealed temperature is increased to 750 °C, the film presented a hexagonal phase. The S2 sample grown at 720 °C maintained a small of  $\gamma$ -monoclinic phase mixed with a hexagonal phase. The morphology of films differs significantly, depending on the grown and annealed conditions. The film grown at 600 °C shows a nanoneedles surface image. A further annealing of the S1 sample at high temperature, the surface became nanostructured, porous, and finally presented long nanowires due to surface oxidation. The Fe-doped  $\text{WO}_3$  samples deposited various temperatures, showing a continuous transformation from nanoneedles to nanowires grown on nanobands. At a temperature of 750 °C a porous surface morphology nanobands is formed. Regarding the S2 sample grown at 720 °C, the surface image shows thin nanowires and nanobands. An annealing of this sample at 750 °C changed the surface in broad nanobands. The EDX mapping show a similar elemental composition in the long nanowires and large

nanobands, particularly W and O. The formation of long nanowires and broad nanobands during annealing under oxygen was supposed to be done by nucleation center generated due to the oxygen migration on the surface. The main Raman peak of the  $\text{WO}_3$  thin film is located at  $810 \text{ cm}^{-1}$  at  $600^\circ\text{C}$  being large than the peaks for the S1 and S2 samples. A sharp Raman peak located at  $810 \text{ cm}^{-1}$  is observed for the S2 sample grown at  $720^\circ\text{C}$ . At high annealing temperature of  $750^\circ\text{C}$ , the Raman peaks of S1 and S2 samples are shifted with  $21 \text{ cm}^{-1}$  unlike to the Fe-doped  $\text{WO}_3$  films grown and annealed at  $720^\circ\text{C}$ . This shift was supposed to be of Fe as a dopant or to the hexagonal phase. The S2 sample grown at  $720^\circ\text{C}$  shows the lattice vibration mode at  $136 \text{ cm}^{-1}$ . Diffraction planes or Raman peaks associated to iron or iron oxides are not present in these measurements. The optical band gap of Fe-doped  $\text{WO}_3$  films was found to decrease with increasing of annealing temperatures. This decrease might be done to the crystalline small cell distortion by Fe doping, either to large oxidation sample surface due to annealing at  $750^\circ\text{C}$  which also increased the grain sizes. These results are useful in understanding the influence of Fe on the morphology surface and on the optical band gap at various deposition and annealed parameters in studying the applicability of the obtained thin film as an active membrane for gas sensor.

**Author Contributions:** Conceptualization, N.C. and M.O.; investigation, M.O. and M.J.; resources, X.X.; data curation, M.J.; validation, M.O. and N.C.; methodology, N.C.; writing—original draft preparation, M.O.; writing—review and editing, M.O. All authors have read and agreed to the published version of the manuscript.

**Funding:** This research was funded by Romanian National Authority for Scientific Research, UEFISCDI: project no. PCCDI 15; project name manufacture, calibration and testing of advanced integrated sensor systems for societal security.

**Conflicts of Interest:** The authors declare no conflict of interest.

## References

1. Di Pietrantonio, F.; Bennett, M.; Cannata, D.; Verona, E.; Palla-Papavlu, A.; Dinca, V.; Dinescu, M.; Mattle, T.; Lipert, T. Volatile toxic compound detection by surface acoustic wave sensor array coated with chemoselective polymers deposited by laser induced forward transfer: Application to sarin. *Sens. Actuators B* **2012**, *174*, 158–167. [[CrossRef](#)]
2. Song, H.; Li, Y.; Lou, Z.; Xiao, M.; Hu, L.; Ye, Z.; Zhu, L. Synthesis of Fe-doped  $\text{WO}_3$  nanostructures with high visible-light-driven photocatalytic activities. *Appl. Catal. B* **2015**, *166–167*, 112–120. [[CrossRef](#)]
3. Miao, R.Y.; Zeng, W.; Gao, Q. SDS-assisted hydrothermal synthesis of NiO flake flower architectures with enhanced gas-sensing properties. *Appl. Surf. Sci.* **2016**, *384*, 304–310. [[CrossRef](#)]
4. Jiang, R.B.; Li, B.X.; Fang, C.H.; Wang, J.F. Metal/semiconductor hybrid nanostructures for plasmon-enhanced applications. *Adv. Mater.* **2014**, *26*, 5274–5309. [[CrossRef](#)]
5. Qin, Y.X.; Cui, M.Y.; Ye, Z.H. Adsorption of ethanol on  $\text{V}_2\text{O}_5$  (010) surface for gas sensing applications: Ab initio investigation. *Appl. Surf. Sci.* **2016**, *379*, 497–504. [[CrossRef](#)]
6. Liu, L.; Song, P.; Yang, Z.; Wang, Q. Highly sensitive and selective trimethylamine sensors based on  $\text{WO}_3$  nanorods decorated with Au nanoparticles. *Phys. E* **2017**, *90*, 109–115. [[CrossRef](#)]
7. Palla-Papavlu, A.; Filipescu, M.; Schneider, C.W.; Antohe, S.; Ossi, P.M.; Radnóczki, G.; Dinescu, M.; Wokaun, A.; Lipert, T. Direct laser deposition of nanostructured tungsten oxide for sensing applications. *J. Phys. D Appl. Phys.* **2016**, *49*, 205101. [[CrossRef](#)]
8. Koltypin, Y.; Nikitenko, S.I.; Gedanken, A. The sonochemical preparation of tungsten oxide nanoparticles. *J. Mater. Chem.* **2002**, *12*, 1107–1110. [[CrossRef](#)]
9. Santato, C.; Odziemkowski, M.; Ulmann, M.; Augustynski, J. Crystallographically oriented mesoporous  $\text{WO}_3$  films: Synthesis, characterization, and applications. *J. Am. Chem. Soc.* **2001**, *123*, 10639–10649. [[CrossRef](#)] [[PubMed](#)]
10. Liu, Z.; Liu, B.; Xie, W.; Li, H.; Zhou, R.; Li, Q.; Wang, T. Enhanced selective acetone sensing characteristics based on Co-doped  $\text{WO}_3$  hierarchical flower-like nanostructures assembled with nanoplates. *Sens. Actuators* **2016**, *235*, 614–621. [[CrossRef](#)]

11. Lee, I.; Choi, S.J.; Park, K.M.; Lee, S.S.; Choi, S.; Kim, D.; Park, C.O. The stability, sensitivity and response transients of ZnO SnO<sub>2</sub> and WO<sub>3</sub> sensors under acetone, toluene and H<sub>2</sub>S environments. *Sens. Actuators* **2014**, *197*, 300–307. [[CrossRef](#)]
12. Kruefu, V.; Wisitsoraat, A.; Tuantranont, A.; Phanichphant, S. Ultra-sensitive H<sub>2</sub>S sensors based on hydrothermal/impregnation-made Ru-functionalized WO<sub>3</sub>nanorods. *Sens. Actuators* **2015**, *215*, 630–636. [[CrossRef](#)]
13. Park, S.; Kim, H.; Jin, C.; Choi, S.-W.; Kim, S.S.; Lee, C. Enhanced CO gas sensing properties of Pt-functionalized WO<sub>3</sub>nanorods. *Thermochim. Acta* **2012**, *542*, 69–73. [[CrossRef](#)]
14. Kim, N.H.; Choi, S.J.; Yang, D.J.; Bae, J.; Park, J.; Kim, I.D. Highly sensitive and selective hydrogen sulfide and toluene sensors using Pd functionalized WO<sub>3</sub>nanofibers for potential diagnosis of halitosis and lung cancer. *Sens. Actuators* **2014**, *193*, 574–581. [[CrossRef](#)]
15. Zhang, Y.; He, W.; Zhao, H.; Li, P. Template-free to fabricate highly sensitive and selective acetone gas sensor based on WO<sub>3</sub> microspheres. *Vacuum* **2013**, *95*, 30–34. [[CrossRef](#)]
16. Liu, X.; Zhang, J.; Yang, T.; Guo, X.; Wu, S.; Wang, S. Synthesis of Pt nanoparticles functionalized WO<sub>3</sub> nanorods and their gas sensing properties. *Sens. Actuators* **2011**, *156*, 918–923. [[CrossRef](#)]
17. Tesfamichael, T.; Ponzoni, A.; Ahsan, M.; Faglia, G. Gas sensing characteristics of Fe-doped tungsten oxide thin films. *Sens. Actuators B* **2012**, *168*, 345–353. [[CrossRef](#)]
18. Liu, B.; Cai, D.; Liu, Y.; Li, H.; Weng, C.; Zeng, G.; Li, Q.; Wang, T. High-performance room-temperature hydrogen sensors based on combined effects of Pd decoration and Schottky barriers. *Nanoscale* **2013**, *5*, 2505–2510. [[CrossRef](#)]
19. Upadhyaya, S.B.; Mishra, R.K.; Sahay, P.P. Enhanced acetone response in co-precipitated WO<sub>3</sub> nanostructures upon indium doping. *Sens. Actuators* **2015**, *209*, 368–376. [[CrossRef](#)]
20. Renitta, A.; Vijayalakshmi, K. A novel room temperature ethanol sensor based on catalytic Fe activated porous WO<sub>3</sub> microspheres. *Catal. Commun.* **2016**, *73*, 58–62. [[CrossRef](#)]
21. Sun, J.; Guo, J.; Ye, J.; Song, B.; Zhang, K.; Bai, S.; Luo, R.; Li, D.; Chen, A. Synthesis of Sb doping hierarchical WO<sub>3</sub> microspheres and mechanism of enhancing sensing properties to NO<sub>2</sub>. *J. Alloys Compd.* **2017**, *692*, 876–884. [[CrossRef](#)]
22. Shen, J.Y.; Wang, M.D.; Wang, Y.F.; Hu, J.Y.; Zhu, Y.; Zhang, Y.X.; Li, Z.J.; Yao, H.C. Iron and carbon codoped WO<sub>3</sub> with hierarchical walnut-like microstructure for highly sensitive and selective acetone sensor. *Sens. Actuators B Chem.* **2018**, *256*, 27–37. [[CrossRef](#)]
23. Yin, M.; Yu, L.; Liu, S. Synthesis of Ag quantum dots sensitized WO<sub>3</sub> nanosheets and their enhanced acetone sensing properties. *Mater. Lett.* **2017**, *186*, 66–69. [[CrossRef](#)]
24. Miu, D.; Birjega, R.; Viespe, C. Surface Acoustic Wave Hydrogen Sensors Based on Nanostructured Pd/WO<sub>3</sub> Bilayers. *Sensors* **2018**, *18*, 3636. [[CrossRef](#)] [[PubMed](#)]
25. Wu, Q.; Huang, J.; Li, H. Deposition of porous nano-WO<sub>3</sub> coatings with tunable grain shapes by liquid plasma spraying for gas-sensing applications. *Mater. Lett.* **2015**, *141*, 100–103. [[CrossRef](#)]
26. Yanga, X.; Sallesa, V.; Kanetib, Y.V.; Liuc, M.; Maillarda, M.; Journeta, C.; Jiangc, X.; Brioude, A. Fabrication of highly sensitive gas sensor based on Au functionalized WO<sub>3</sub> composite nanofibers by electrospinning. *Sens. Actuators* **2015**, *220*, 1112–1119. [[CrossRef](#)]
27. Stoycheva, T.; Annanouch, F.E.; Gràcia, I.; Llobet, E.; Blackman, C.; Correig, X.; Vallejos, S. Micromachined gas sensors based on tungsten oxide nanoneedles directly integrated via aerosol assisted CVD. *Sens. Actuators B* **2014**, *198*, 210–218. [[CrossRef](#)]
28. Chi, X.; Liu, C.; Liu, L.; Li, Y.; Wang, Z.; Bo, X.; Liu, L.; Su, C. Tungsten trioxide nanotubes with high sensitive and selective properties to acetone. *Sens. Actuators* **2014**, *194*, 33–37. [[CrossRef](#)]
29. Upadhyay, S.B.; Mishra, R.K.; Sahay, P.P. Cr-dopedWO<sub>3</sub> nanosheets: Structural, optical and formaldehyde sensing properties. *Ceram. Int.* **2016**, *42*, 15301–15310. [[CrossRef](#)]
30. Zhang, L.; Tang, X.; Lu, Z.; Wang, Z.; Li, L.; Xia, Y. Facile synthesis and photocatalytic activity of hierarchical WO<sub>3</sub> core–shell microspheres. *Appl. Surf. Sci.* **2011**, *258*, 1719–1724. [[CrossRef](#)]
31. Righetto, M.; Tricoli, A.; Gass, S.; Schmid, A.; Amann, A.; Pratsinis, S.E. Breath acetone monitoring by portable Si: WO<sub>3</sub> gas sensors. *Anal. Chim. Acta* **2012**, *738*, 69–75. [[CrossRef](#)] [[PubMed](#)]
32. Salthammer, T.; Mentese, S.; Marutzky, R. Formaldehyde in the indoor environment. *Chem. Rev.* **2010**, *110*, 2536–2572. [[CrossRef](#)]

33. Chung, P.; Tzenmg, C.; Ke, M.; Lee, C. Formaldehyde gas sensor: A review. *Sensors* **2013**, *13*, 4468–4484. [[CrossRef](#)] [[PubMed](#)]
34. Salthammer, T. Formaldehyde in the ambient atmosphere: From indoor pollutant to an outdoor pollutant. *Angew. Chem. Int.* **2013**, *52*, 3320–3327. [[CrossRef](#)] [[PubMed](#)]
35. Chang, C.T.; Lin, K.L. Assessment of the strategies for reducing VOCs emission from polyarea-formaldehyde resin synthetic fiber leather industry in Taiwan. *Resour. Conserv. Recycl.* **2006**, *46*, 321–334. [[CrossRef](#)]
36. Leonardi, S.G.; Mirzaei, A.; Bonavita, A.; Santangelo, S.; Frontera, P.; Pantò, F.; Antonucci, P.L.; Neri, G. A comparison of the ethanol sensing properties of iron oxide nanostructures prepared via the sol–gel and electrospinning techniques. *Nanotechnology* **2016**, *27*, 075502. [[CrossRef](#)]
37. Mirzaei, A.; Park, S.; Sun, G.J.; Kheel, H.; Lee, C.; Lee, S. Fe<sub>2</sub>O<sub>3</sub>/Co<sub>3</sub>O<sub>4</sub> composite nanoparticle ethanol sensor. *J. Korean Phys. Soc.* **2016**, *69*, 373–380. [[CrossRef](#)]
38. Jelle, B.P.; Georg, H. Performance of an electrochromic window based on polyaniline, prussian blue and tungsten oxide. *Sol. Energy Mater. Sol.* **1999**, *58*, 277–286. [[CrossRef](#)]
39. Choi, S.; Bonyani, M.; Sun, G.J.; Lee, J.K.; Hyun, S.K.; Lee, C. Cr<sub>2</sub>O<sub>3</sub> nanoparticle-functionalized WO<sub>3</sub> nanorods for ethanol gas sensors. *Appl. Surf. Sci.* **2018**, *432*, 241–249. [[CrossRef](#)]
40. Huang, S.; Wang, T.; Xiao, Q. Effect of the Fe doping on the structures and gas sensing properties of ZnO porous microspheres. *J. Phys. Chem. Solids* **2015**, *76*, 51–58. [[CrossRef](#)]
41. Szilagyi, I.M.; Madarasz, J.; Pokol, G.; Kiraly, P.; Tarkanyi, G.; Saukko, S.; Mizsei, J.; Toth, A.L.; Szabo, A.; Varga-Josepovit, K. Stability and Controlled Composition of Hexagonal WO<sub>3</sub>. *Chem. Mater.* **2008**, *20*, 4116–4125. [[CrossRef](#)]
42. Ahsan, M.; Tesfamichael, T.; Ionescu, M.; Bell, J.; Motta, N. Low temperature CO sensitive nanostructured WO<sub>3</sub> thin films doped with Fe. *Sens. Actuators B Chem. Sens. Actuators* **2012**, *162*, 14–21. [[CrossRef](#)]
43. Datta, N.; Ramgir, N.; Kaur, M.; Roy, M.; Bhatt, R.; Kailasaganapathi, S.; Debnath, A.K.; Aswal, D.K.; Gupta, S.K. Vacuum deposited WO<sub>3</sub> thin films based sub-ppm H<sub>2</sub>S sensor. *Mater. Chem. Phys.* **2012**, *134*, 851–857. [[CrossRef](#)]
44. Manciu, F.S.; Enriquez, J.L.; Durrer, W.G.; Yun, Y.; Chintalapalle, V.R.; Gullapalli, S.K. Spectroscopic analysis of tungsten oxide thin films. *J. Mater. Res.* **2010**, *25*, 2401–2406. [[CrossRef](#)]



© 2020 by the authors. Licensee MDPI, Basel, Switzerland. This article is an open access article distributed under the terms and conditions of the Creative Commons Attribution (CC BY) license (<http://creativecommons.org/licenses/by/4.0/>).